

Photocatalytic Water Splitting Reaction Catalyzed by Ion-Exchanged Salts of Potassium Poly(heptazine imide) 2D Materials

Sudhir K. Sahoo, Ivo F. Teixeira, Aakash Naik, Julian Heske, Daniel Cruz, Markus Antonietti, Aleksandr Savateev, and Thomas D. Kühne*

Cite This: *J. Phys. Chem. C* 2021, 125, 13749–13758

Read Online

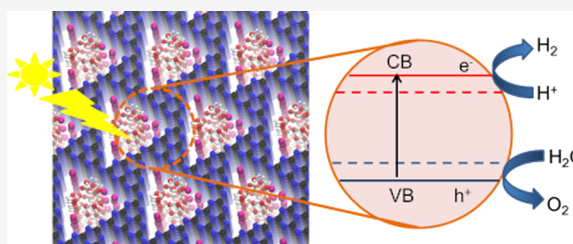
ACCESS |

Metrics & More

Article Recommendations

Supporting Information

ABSTRACT: Potassium poly (heptazine imide) (K-PHI), a crystalline two-dimensional carbon–nitride material, is an active photocatalyst for water splitting. The potassium ions in K-PHI can be exchanged with other ions to change the properties of the material and eventually to design the catalysts. We report here the electronic structures of several ion-exchanged salts of K-PHI (K, H, Au, Ru, and Mg) and their feasibility as water splitting photocatalysts, which were determined by density functional theory (DFT) calculations. The DFT results are complemented by experiments where the performances in the photocatalytic hydrogen evolution reaction (HER) were recorded. We show that due to its narrow band gap, Ru-PHI is not a suitable photocatalyst. The water oxidation potentials are straddled between the band edge potentials of H-PHI, Au-PHI, and Mg-PHI; thus, these are active photocatalysts for both the oxygen and hydrogen evolution reactions, whereas K-PHI is active only for the HER. The experimental data show that these are active HER photocatalysts, in agreement with the DFT results. Furthermore, Mg-PHI has shown remarkable performance in the HER, with a rate of 539 $\mu\text{mol}/(\text{h}\cdot\text{g})$ and a quantum efficiency of 7.14% at 410 nm light irradiation, which could be due to activation of the water molecule upon adsorption, as predicted by our DFT calculations.



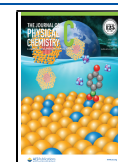
INTRODUCTION

Photocatalytic water splitting is foreseen as a clean, green, and sustainable alternative to the utilization of fossil fuels.^{1–4} In this reaction, solar energy received in the form of light is converted into the driving force to enable the endothermic chemical reaction and is eventually stored in a chemical bond. The energy may be released upon oxidation of the solar fuel. The splitting of water into hydrogen (H_2) and oxygen (O_2) is a thermodynamically unfavorable process that entails an enthalpy of 1.23 eV.^{5–8} It requires a suitable catalyst to absorb the solar light energy and drive the overall reaction. The H_2 gas from water splitting is a source of clean energy, as well as a carbon-neutral fuel, which only releases water upon combustion and thus does not cause harm to the environment. According to a general photocatalytic mechanism of water splitting, in the first step, the catalyst absorbs sunlight, which excites electrons to move from the valence band to the conduction band. The holes (h^+) generated in the valence band then react with the water molecule to form O_2 , while the electrons (e^-) in the conduction band combine with protons to form H_2 .⁹ It has been stated that the total amount of solar energy received by the earth in 1 h is sufficient to meet the annual global energy consumption.¹⁰ Awareness of this has led to an enormous quest by many interested members of the scientific community for a photocatalyst that promotes efficient water splitting. A suitable photocatalyst should have the following two most important properties: (a) a band gap larger

than 1.23 eV for the material and (b) suitable band edge potentials, i.e., the valence band edge potential should be more positive than the water oxidation potential and the conduction band edge potential be more negative than the hydrogen evolution potential.¹¹ The transition-metal (TM) oxides, phosphides, and sulfides, as well as supported TM clusters including noble metals, have demonstrated success as photocatalysts in this important reaction.^{12–14} Interestingly, graphitic nitrogen-doped carbons are porous materials that, as metal-free water splitting photocatalysts, offer the advantages of physical and chemical stability in water, suitable band gap and band edge positions, and cost-effectiveness due to the use of earth-abundant elements.^{15–18}

A new class of nitrogen-doped carbons or carbon nitrides, the potassium poly (heptazine imides), denoted K-PHI, have recently been synthesized by Savateev et al., and they have shown excellent photocatalytic activity in water splitting reactions, as well as organic reactions.^{19,20} Interestingly, the X-ray diffraction patterns in combination with density functional theory (DFT) studies indicate that K-PHI is

Received: May 3, 2021
 Revised: May 27, 2021
 Published: June 16, 2021



crystalline in nature, and the positively charged K ions between the PHI layers can be envisaged as a frustrated Lewis pair-like structure, which we termed “frustrated Coulomb pair” (FCP).²¹ Further, the presence of ions improves the long-range structural order, which is beneficial for photocatalytic applications. Hence, PHI-based catalysts performed better than g-C₃N₄ in the hydrogen evolution reaction (HER), as reported by Chen et al.²² It has also been experimentally proven that the ions intercalated in the PHI scaffolds can be exchanged with other ions, such as proton (H⁺), sodium (Na⁺), magnesium (Mg²⁺), gold (Au⁺ or Au³⁺), and ruthenium (Ru²⁺ or Ru³⁺), by dispersing the parent material in an aqueous solution of the corresponding metal salt, without much affecting the crystal structure.²³ Therefore, this ion-exchange process can be utilized to engineer the band gap and band edges of the material, while preserving the crystal structure. It is important to highlight that the efficiency of the photocatalysts can be further improved by engineering the band gap of the material. For example, if the band gap is reduced, then the material can absorb photon in the visible range. This can be achieved by either doping^{24–26} or manipulating the side chains/functional groups as in the covalent organic frameworks.^{27,28} It has been also reported that doping of g-C₃N₄ improves its photocatalytic activity in the water splitting reactions.^{29,30} However, to the best of our knowledge, there is no systematic study on the effect of extra-framework cations on the band gap of PHI-based materials. In this paper, we employed DFT-based calculations to study the electronic structures of K-PHI and systems, where K⁺ is replaced by H, Au⁺, Mg²⁺, and Ru³⁺, as well as the applicability of these materials in the photocatalysis of water splitting reactions. The DFT results are complemented by experiments in which these materials are synthesized, characterized and their photocatalytic activities are assessed in the hydrogen evolution.

METHOD

Computational Details. All DFT calculations were carried out using the projector augmentation plane-wave (PAW) method,³¹ as implemented in the Vienna Ab initio Simulation Package (VASP).^{32–34} The Perdew–Burke–Ernzerhof (PBE)³⁵ exchange–correlation functional together with Grimme’s empirical dispersion correction (D3)³⁶ was employed to optimize the structures. The Kohn–Sham orbitals were expanded using a plane-wave basis set with an energy cutoff of 350 eV. In our DFT calculations, the valence states 1s for H, 2s2p for C, 2s2p for N, 3s3p for Mg, 3p4s for K, 4d5s for Ru, and 5d6s for Au were treated explicitly. The Brillouin zone was sampled using a 2 × 2 × 4 Monkhorst–Pack *k*-point grid.³⁷ The structures were optimized using the conjugate gradient method until the ionic forces were less than 0.01 eV/Å. It is well known that generalized gradient approximation (GGA) functionals such as PBE underestimate the band gap of materials. This can be improved using hybrid functionals such as HSE;³⁸ however, the computational expense increases. Therefore, in our calculations, the structures were optimized at the PBE level. A total energy calculation using the HSE functional was performed to determine the band gap. The default value for parameter α of 0.25 was used to include 25% of the Hartree–Fock exchange energy.

In addition to a suitable band gap, the photocatalyst should have band edges positioned such that both the valence band maximum (VBM) and the conduction band minimum (CBM)

straddle the hydrogen and oxygen reduction potentials. The positions of the VBM and the CBM are calculated³⁹ by

$$E_{\text{VBM}} = E_{\text{BGC}} - \frac{1}{2}E_{\text{g}} \quad (1a)$$

$$E_{\text{CBM}} = E_{\text{BGC}} + \frac{1}{2}E_{\text{g}} \quad (1b)$$

where E_{g} is the band gap of the material, which is computed using the HSE DFT functional,³⁸ and E_{BGC} is the energy of the band gap center (BGC) relative to vacuum. The BGC is located at the center of the eigenvalues of the VBM and CBM obtained using a periodic slab model with a vacuum of 10 Å, i.e., a surface. The position of the BGC with reference to vacuum is obtained by taking the difference between the electrostatic potential in the vacuum region and the BGC energy using the HSE functional.

In our calculation, the M-PHI model contains one atomic layer and the experimental lattice parameters $a = b = 12.5$ Å, $c = 3.2$ Å, $\alpha = \beta = 90.0^\circ$, and $\gamma = 120.0^\circ$. Here, M represents any metal ion or a hydrogen atom. The effect of the interlayer distance on the electronic structure and the band gap was computed by varying the value c , while the other lattice parameters were fixed at the original values. The H-PHI model contains three H atoms to obtain a neutral system. They were replaced by three K⁺ ions and three Au⁺ ions in K-PHI and Au-PHI, respectively, so that these are charge neutral. Accordingly, two H atoms of H-PHI were replaced by one Mg²⁺ ion to obtain a neutral Mg-PHI and all three H atoms were replaced by one Ru³⁺ ion for Ru-PHI. In H-PHI, K-PHI, and Au-PHI, the concentration of the dopants is equal to 9.3 atom %. The concentrations of the corresponding ions (dopants) in Mg-PHI and Ru-PHI, however, are 3.2 and 3.3 atom %, respectively.

Photocatalytic Water Splitting Reaction. In general, the photocatalytic water splitting reaction is viewed as a combination of two half-cell reactions.^{40,41} The oxygen evolution reaction (OER) is modeled in a successive four-electron transfer process as follows

- A: * + H₂O → HO* + H⁺ + e⁻
- B: HO* → O* + H⁺ + e⁻
- C: O* + H₂O → HOO* + H⁺ + e⁻
- D: HOO* → * + O₂ + H⁺ + e⁻

Here, * represents the surface site, where the reactant or reagent or species, etc., is adsorbed. H*, HO*, O*, and HOO* denote H, HO, O, and HOO species adsorbed on the surface site *, respectively.

Similarly, the hydrogen evolution reaction (HER) will occur on the surface in a successive two-electron transfer as follows:

- E: * + H⁺ + e⁻ → H*
- F: H* + H⁺ + e⁻ → * + H₂

To understand the thermodynamics of the photocatalytic water splitting reaction, the free energy of the elementary steps (A–F) was computed using the computational hydrogen electrode (CHE) techniques proposed by Nørskov et al.⁴² as

$$\Delta G = \Delta E + \Delta ZPE - T\Delta S - eU - kT \times \text{pH} \times \ln 10 \quad (2)$$

where ΔE is the reaction energy, i.e., the potential energy difference computed using DFT calculations. The temperature of the system T was set to 300 K. Since the contribution of pH to the free energy is a constant shift, it was set to zero. In eq 2,

Δ ZPE represents the difference in the zero point energy and S is the entropy. For the surface and the intermediates adsorbed on the surface, the entropy S is approximated as the vibrational entropy S_{vib} . In our vibrational frequency calculations, all of the atoms, including the surface ones, were considered. For gas-phase molecules (H_2 , O_2 , and H_2O), however, the entropy values were taken from the corresponding thermochemical data.⁴³ Further, in eq 2, e is the number of electrons and U is the bias potential, which is calculated such that each of the elementary steps is thermodynamically favorable.

Experimental Details. K-PHI Synthesis. A mixture of 5-aminotetrazole (0.99 g) and LiCl/KCl eutectics (2.236 g LiCl/2.733 g KCl) was ground in a ball mill for 5 min at the operational frequency of 25 Hz. The resultant flour-like white powder was transferred to a 15 mL porcelain crucible, which was then covered with a porcelain lid and placed in an oven. The temperature inside the oven was increased from 20 to 600 °C within 4 h (2.4 K min⁻¹) under a flow of nitrogen (15 L min⁻¹), after which it was maintained at 600 °C for another 4 h. After that, the oven was allowed to slowly cool to room temperature. The melt from the crucible was transferred to a beaker, and deionized water (50 mL) and a stir bar were added. The suspension was stirred at room temperature for 4 h until it became homogeneous and no agglomerated particles were seen. The solid was separated by centrifugation (8400 min⁻¹, 5 min). The solid was washed with water (3 × 1.5 mL) using a centrifuge (13 500 min⁻¹, 3 min) and dried under vacuum at 60 °C.

Preparation of the M-PHI Samples. To 2 mL of a concentrated solution of the metal chloride (HAuCl_4 : 2.0 mol L⁻¹; RuCl_3 : 2.0 mol L⁻¹; MgCl_2 : 5.7 mol L⁻¹), 100 mg of K-PHI was added. The mixture was sonicated for 30 min and then separated by centrifugation (13 500 min⁻¹, 3 min). The obtained solid was washed with deionized water (3 × 2.0 mL) and dried under vacuum at 60 °C. The protonated sample (H-PHI) was prepared similarly. To 2 mL of concentrated HCl (12 mol L⁻¹), 100 mg of K-PHI was added. The mixture was sonicated for 30 min and then separated by centrifugation (13 500 min⁻¹, 3 min). The obtained solid was washed with deionized water (1 × 2.0 mL) and dried under vacuum at 60 °C.

Characterization. The synthesized samples were characterized by X-ray diffraction, steady-state absorption spectroscopy, and X-ray and ultraviolet photoelectron spectroscopy (UPS). The diffraction patterns were recorded on a Bruker D8 Advance diffractometer equipped with a scintillation counter detector with Cu $K\alpha$ radiation ($\lambda = 0.15418$ nm), applying a 2θ step size of 0.05° and a counting time of 3s per step. Steady-state UV–vis absorption spectra were acquired using a Shimadzu UV 2600 equipped with integrating sphere in transmission mode. The UPS spectra were acquired with a He I (21.2 eV) radiation source. The detector was a Combined Lens and Analyzer Module (CLAM) from Thermo VG.

Hydrogen Evolution Reaction. Photocatalytic activities of the prepared materials in the H_2 evolution were evaluated in a closed system equipped with a pressure detector to record the pressure buildup during the HER. All of the prepared photocatalysts were tested using the same set of light-emitting diodes (LEDs) as irradiation source: white LED light (50 W), 410 nm (50 W), and 465 nm (50 W). The volume of the reaction mixture was 38 mL, and the temperature was maintained at 298 K by water cooling. The amounts of the evolved gases were finally calculated by the Clausius–

Clapeyron relation ($PV = nRT$). Typically, 50 mg of the solid catalyst was dispersed in 38 mL of a DI water and TEOA (10 vol %) mixture. Before mixing in the reaction chamber, DI water and TEOA were degassed by sonication in vacuum. For the deposition of Pt cocatalysts, 39.4 μL of 8 wt % H_2PtCl_6 solution was added into the reaction medium. Theoretically, it should give 3 wt % Pt deposited at the catalyst; however, we have measured the actual concentration of Pt by ICP after the reaction, which was found to be 0.5–1.0 wt %. The H_2 evolution apparent quantum yield (AQY) was measured using a monochromatic visible light (420 ± 1.0 nm). The AQY was calculated as follows

$$\text{AQY} (\%) = \frac{2r_{\text{H}_2} N_A h c}{SI\lambda t} \times 100$$

where r_{H_2} is the production rate of H_2 molecules (mol·s⁻¹), N_A is Avogadro's constant, h is Planck's constant, c is the speed of light (3×10^8 m/s), S is the irradiation area (cm²), I is the intensity of irradiation light (W/cm²), t is the photoreaction time (s), and λ is the wavelength of the monochromatic light (m).

RESULTS AND DISCUSSION

Bulk Structure of M-PHI. First, we investigated the bulk structure of M-PHI materials. H-PHI was used as a reference

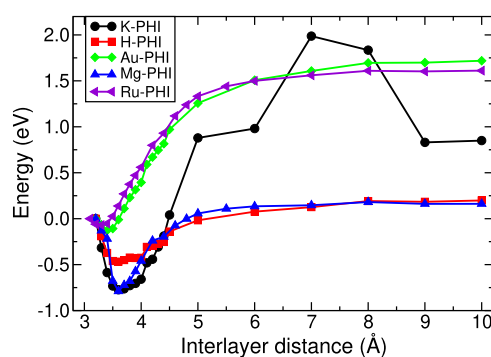


Figure 1. Relative total energy (in eV) as a function of interlayer distance (Å) in M-PHI. The interlayer distances and the bulk structures of the minimum energy configurations are given in Table 1 and Figure S1 in the SI, respectively.

Table 1. Equilibrium Interlayer Distance (in Å) of M-PHI Computed with DFT Using PBE Functional and from PXRD Pattern

| catalyst | d_0 (PBE) | d_0 (experiment) |
|----------|-------------|--------------------|
| K-PHI | 3.6 | 3.14 |
| H-PHI | 3.6 | 3.18 |
| Au-PHI | 3.4 | 3.19 |
| Mg-PHI | 3.6 | 3.16 |
| Ru-PHI | 3.3 | 3.17 |

structure in determining the structure of the relatively more complex M-PHI due to the presence of ions. These ions could occupy positions either in the same plane as PHI or between the PHI layers. In H-PHI, the H atoms are covalently bonded to the N atoms of the PHI scaffold. Our DFT results suggest that in K-PHI, the K^+ ions are present between the PHI layers, while the Au^+ ions are present in the same plane as PHI in Au-PHI, as shown in Figure S1 in the Supporting Information

Table 2. Computed Band Gap (in eV) of M-PHI Using PBE or HSE DFT Functional and Experimentally Measured Optical Band Gap from UV–Vis Spectra

| M-PHI | E_g (PBE) | E_g (HSE) | E_g (experiment) |
|--------|-------------|-------------|--------------------|
| K-PHI | 1.634 | 2.484 | 2.68 |
| H-PHI | 1.647 | 2.544 | 2.90 |
| Au-PHI | 0.821 | 2.083 | 2.47 |
| Mg-PHI | 1.4 | 2.748 | 2.71 |
| Ru-PHI | 0.0 | 0.0 | 0.89 |

(SI). This agrees well with our previous findings.²¹ However, interestingly, our results suggest that the Mg^{2+} ions in Mg-PHI are likely to be present between the PHI layers, whereas in Ru-PHI, the Ru^{3+} ions are in the same plane as PHI (see Figure S1 in the SI). We then varied the interlayer distance and the corresponding total energy was computed, which is shown in Figure 1. Table 1 shows the equilibrium interlayer distance obtained from the DFT calculations. For H-PHI, K-PHI, and Mg-PHI, the minimum energy configuration was found at 3.6 Å. For Au-PHI and Ru-PHI, the minimum energy configurations were found at 3.4 and 3.3 Å, respectively. The

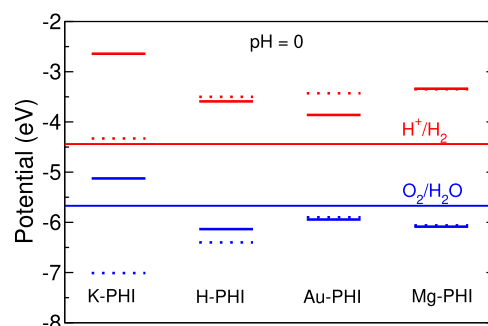


Figure 3. DFT-computed (solid line) and UPS-measured (dashed line) VBM of M-PHI and OER potential (blue). CBM of M-PHI and the HER potential (red).

scanning electron microscopy (SEM) images of the M-PHI samples and $g\text{-C}_3\text{N}_4$, are given in Figure S2 in the SI. The SEM images indicate that the samples have similar morphology, though the metal-exchanged samples seem bulkier, which could be due to the long-range structural order because of the presence of extra-framework cations in the negatively charged

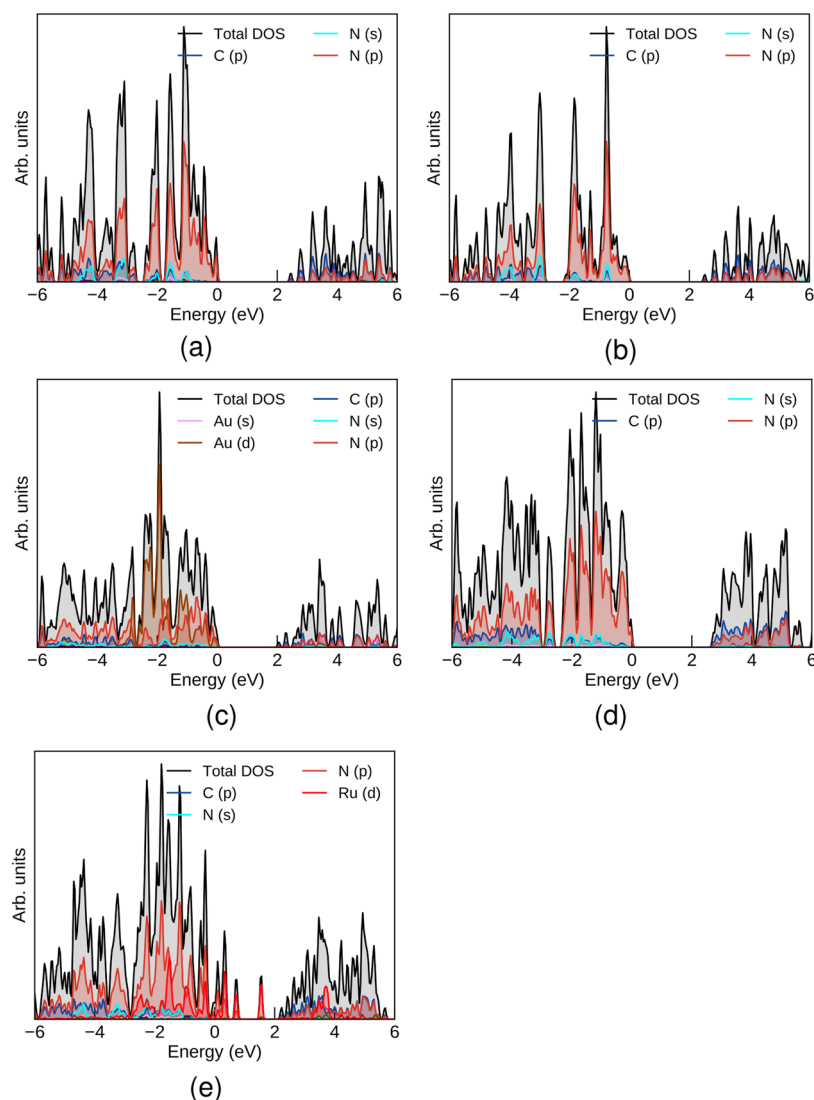
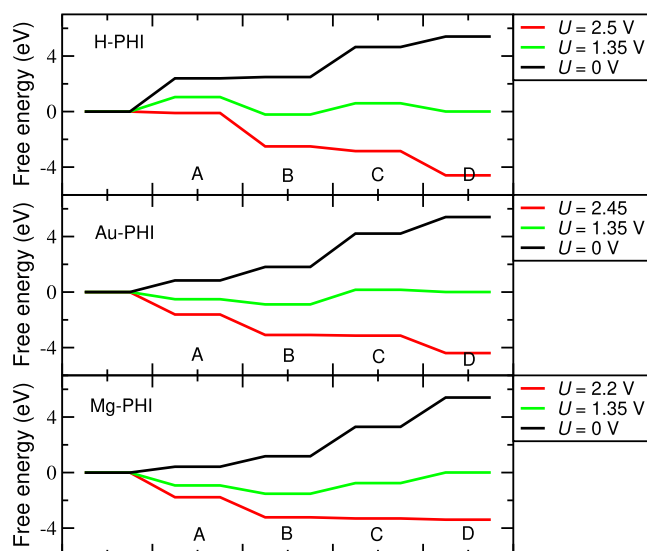


Figure 2. Atom-resolved total density of states (DOS) of K-PHI (a), H-PHI (b), Au-PHI (c), Mg-PHI (d), and Ru-PHI (e) obtained from DFT calculations using hybrid HSE functional.

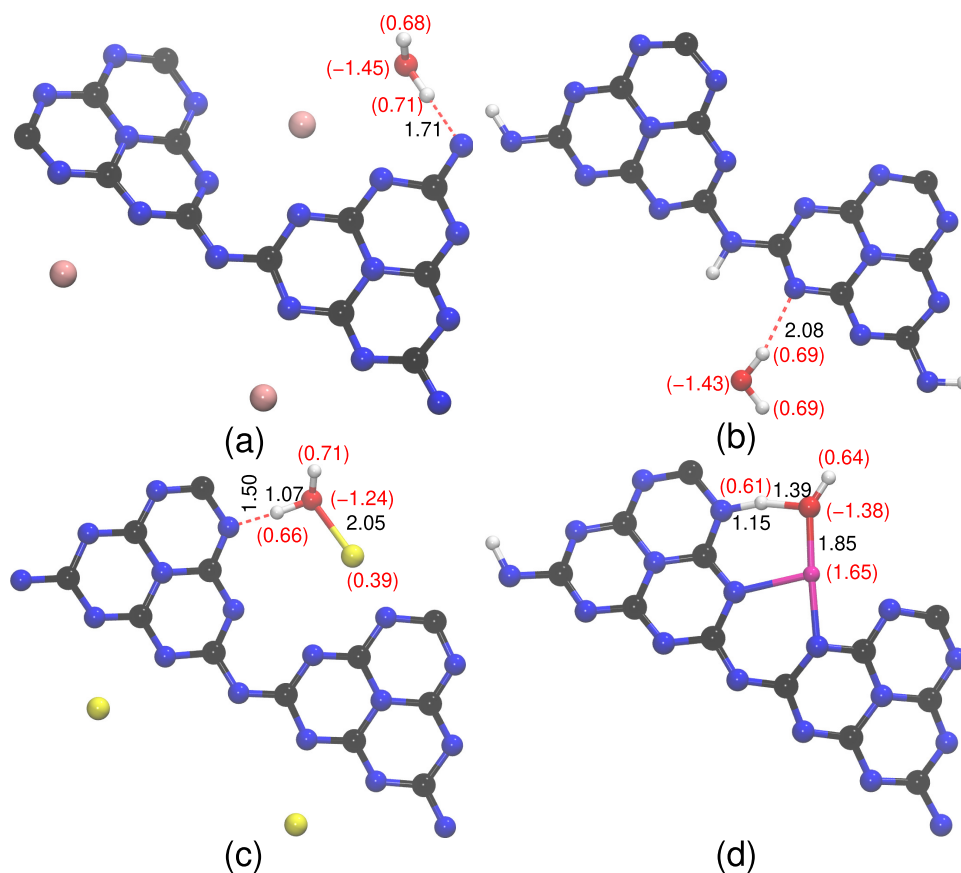
Table 3. Adsorption Energy ΔE_{ads} and Gibbs Free Energy ΔG_{ads} at 300 K of Water Adsorption to the M-PHI Catalyst

| catalysts | ΔE_{ads} (eV) | ΔG_{ads} (eV) |
|-----------|------------------------------|------------------------------|
| K-PHI | -1.32 | -0.92 |
| H-PHI | -0.53 | -0.21 |
| Au-PHI | -1.60 | -0.77 |
| Mg-PHI | -1.93 | -1.39 |

PHI scaffolds. The chemical composition of the M-PHI samples, obtained from energy-dispersive X-ray analysis and elemental analysis, is given in Table S1 in the SI. This infers that the K ions are indeed exchanged by the M ions without any distortion to the PHI scaffold, which can be ascertained from the C/N ratio. Further, our results suggest that 14.9 atom % K in K-PHI, 26.2 atom % Au in Au-PHI, 15.4 atom % Ru in Ru-PHI, and 2.0 atom % Mg in Mg-PHI are present. It is important to note here that in our DFT model, 9.4 atom % K, H, and Au in K-PHI, H-PHI, and Au-PHI, respectively, and 3.2 atom % Mg in Mg-PHI, and 3.3 atom % in Ru-PHI are present. Thus, the DFT results can only be compared qualitatively with the experimental results. The powder X-ray diffraction (PXRD) patterns of M-PHI are shown in Figure S3 in the SI. They indicate that these are all semicrystalline materials. The sharp peak at $2\theta \approx 27^\circ$ observed for M-PHI corresponds to the distance between two successive PHI layers and agrees well with our previous studies on K-PHI.^{21,23} This further highlights the fact that the crystalline structure of M-PHI is

**Figure 5.** Gibbs free energy computed at different bias potentials at 300 K and pH = 0 for OER catalyzed by M-PHI.

intact even after the ion-exchange process. The corresponding interlayer distances in M-PHI obtained from the PXRD patterns are also given in Table 1. The lower interlayer distance observed in K-PHI and Mg-PHI suggests that these are more thermodynamically stable than the rest of the systems studied here. This agrees well with the interlayer distance vs

**Figure 4.** Optimized structure of an isolated H_2O molecule adsorbed on K-PHI (a), H-PHI (b), Au-PHI (c), and Mg-PHI (d) obtained from the DFT calculations. The corresponding adsorption energies are listed in Table 3, and some of the selected bond distances, in Å, are highlighted. The point charges obtained by the Bader charge analysis of some of the selected atoms are given (e unit) in parentheses.

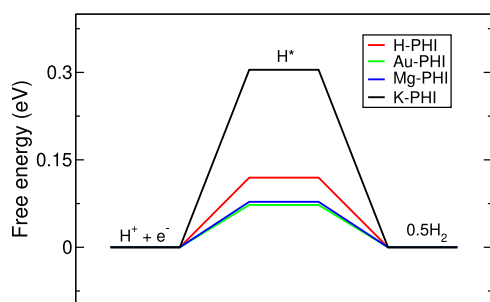


Figure 6. Gibbs free energy computed at 300 K and pH = 0 for the HER catalyzed by M-PHI.

total energy plot, which is shown in Figure 1. Table 1, which compares the experimental interlayer distances with the DFT-calculated values, clearly indicates that the computed distances are overestimated, with a relative error of 4–14%. However, it is well known that the GGA functional is unable to accurately account for dispersion interactions.

Band Gap and Band Alignment of M-PHI. The UV–vis spectra of the M-PHI, which are given in Figure S4 in the SI, show one main absorption band at $\lambda \approx 400$ –450 nm for all of the systems studied here except Ru-PHI. This band can be ascribed to the π – π^* transition in the conjugate heptazine moiety. Another prominent band is observed at 550, 500, and

550 nm for K-PHI, H-PHI, and Mg-PHI, respectively, which corresponds to the n – π^* transition involving the lone pair of the nitrogen (N) atom. However, this band is red-shifted for Au-PHI (Au^{3+}) and is observed at 675 nm. The computed DFT band gaps of the M-PHI using a PBE or hybrid HSE functional together with the experimentally measured optical band gaps obtained from the Tauc plots of the UV–vis absorption spectra are listed in Table 2. As expected, the band gaps obtained from DFT calculations using the PBE functional are underestimated. When using the hybrid HSE functional, the values are much higher and are close to the experimental values. It is important to note here that ideal models with perfect stoichiometry have been used in the DFT calculation, whereas in experiment, the chemical composition within the material may vary due to variation in metal content. Therefore, the DFT results can only be qualitatively compared with the experimental results. To catalyze the water splitting reaction, the band gap of the photocatalyst should be larger than 1.23 eV. Since the band gap of Ru-PHI was found to be zero using the HSE functional, and the experimental value 0.89 eV, it would not be a suitable photocatalyst for water splitting. Hence, it has been excluded from our further DFT calculations. The DFT-calculated and experimentally measured band gaps of K-PHI, H-PHI, Au-PHI, and Mg-PHI were found to be larger than 1.23 eV. This indicates that these four systems are potentially suitable for water splitting reactions.

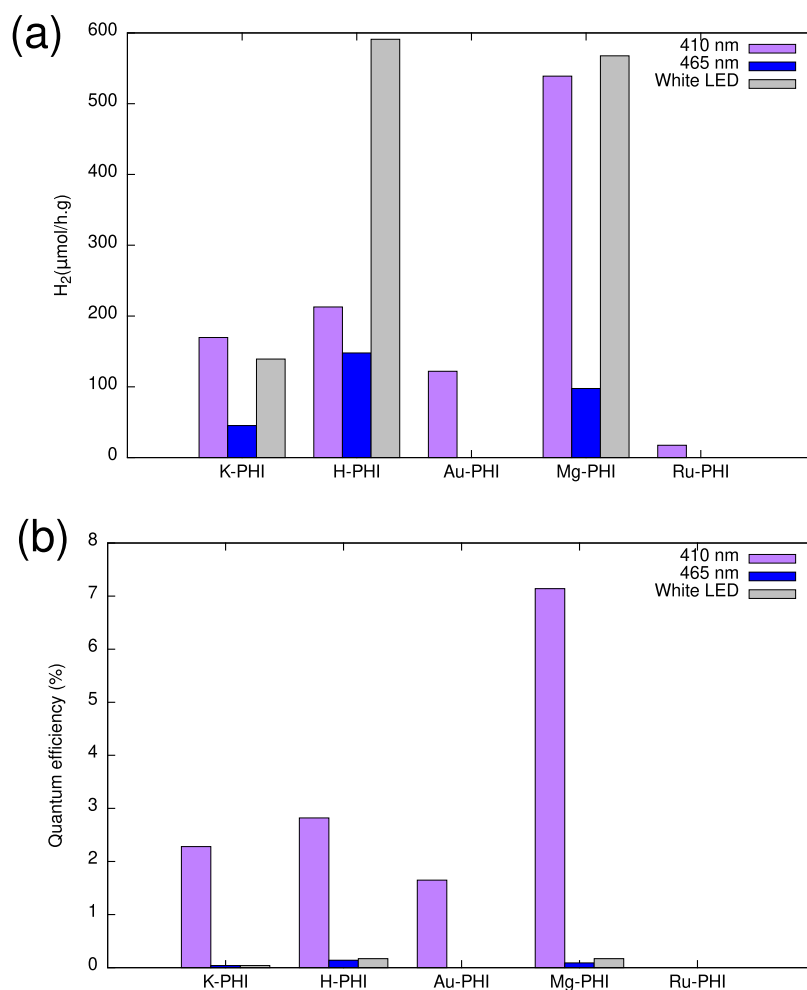


Figure 7. Performance of M-PHI as a HER photocatalyst: (a) rate of H₂ evolution and (b) quantum efficiency.

To understand the effect of the extra-framework atoms/ions on the band gap of M-PHI, we looked into the atom-resolved total density of states (DOS), as shown in Figure 2. In both K-PHI and H-PHI, the valence band arises mainly from 2p orbitals of N atoms and the conduction band from 2p orbitals of C atoms as shown in Figure 2a,2b, respectively. However, our results suggest negligible contribution of H and K atoms to the total DOS of H-PHI and K-PHI, respectively. Figure 2c depicts that in Au-PHI, besides the contributions from C and N atoms that are observed in H-PHI and K-PHI, there are significant contributions from both the s- and d-orbitals of Au atoms to both the valence and the conduction bands. Interestingly, our calculations suggest that the total DOS of Mg-PHI is very similar to that of K-PHI and H-PHI (see Figure 2d). Furthermore, the d-orbitals in Ru-PHI have a contribution in both the valence and conduction band regions, which is the reason why no gap is observed, as shown in Figure 2e. The electronic band structure of M-PHI (M = H, K, Au, and Mg) was then calculated using the hybrid HSE DFT functional, as given in Figure S5 in the SI. Figure S5 in the SI clearly confirms that all of these materials have an indirect band gap. It has been reported that the probability of recombination of photogenerated carriers is lower in materials with an indirect band gap.⁴⁴ Thus, it can now be concluded that M-PHI materials would be suitable photocatalysts.

It has been reported that the HER and OER potentials are -4.44 and -5.67 eV, respectively, at pH = 0 in the vacuum scale.⁴⁵ To determine the feasibility of using M-PHI as the photocatalyst, the band edge positions with respect to vacuum level were evaluated using eqs 1a and 1b. The calculated band edge positions using the hybrid HSE DFT functional are shown in Figure 3 together with those obtained from UPS (see Figure S6 in the SI). Our results predict that H-PHI, Au-PHI, and Mg-PHI would be suitable for both the HER and OER, since their band edges straddle the redox potentials of water. On the other hand, K-PHI would only be suitable for HER according to the DFT calculations, since its valence band edge is found to be above the OER potential. It should be noted here that there is no contribution of H and K atoms to the valence and the conduction bands in the partial DOS projection, as shown in Figure 2. However, it is now quite evident that these atoms definitely play a role in the positioning of the band edges and thus could affect the photocatalytic properties.

An efficient photocatalyst has photogenerated carriers with light masses so that the generated carriers have a higher probability of reaching the surface reaction sites. Furthermore, significant difference in the effective masses of the holes and electrons reduces the probability of carrier recombination. We employed parabolic fitting of the VBM and CBM to calculate the effective hole mass m_h^* and the effective electron mass m_e^* using the SUMO package.⁴⁶ The obtained values of m_h^* and m_e^* along different directions in the Brillouin zone are listed in Table S2 in the SI, which interestingly shows that both requirements are met by all of these PHI-based materials.

Thermodynamics Modeling of Water Splitting Reaction. Water Molecule Adsorption. We first investigated the adsorption of an isolated water molecule on the surface of M-PHI. The corresponding adsorption energy and free energy at 300 K are listed in Table 3, and the atomic structures are shown in Figure 4. Our DFT results suggest that adsorption of a water molecule is thermodynamically favorable at both 0 K and 300 K. Furthermore, the water molecule adsorbs

dissociatively on the Mg-PHI surface, and this entails an adsorption energy of -1.93 eV. The OH group of the water molecule is bonded to the Mg atom, and the H atom is bonded to the N atom of the PHI scaffold, as shown in Figure 4d. Figure 4 also shows the partial charges of some of the selected atoms obtained by the Bader charge analysis. It clearly indicates that there is charge transfer between the H₂O molecule and M-PHI, since the point charge of the oxygen atom changes upon adsorption, compared to that of the isolated molecule ($q_O = -1.40$ e and $q_H = +0.70$ e). The results further suggest that 0.13, 0.06, and 0.05 e charges from Mg-PHI, K-PHI, and H-PHI, respectively, are transferred to the H₂O molecule, whereas 0.13 e charge is transferred from the H₂O molecule to the Au-PHI. It can also be seen from Table 3 that the water adsorption energies for Mg-PHI, Au-PHI, and K-PHI are higher than that for H-PHI. This could be due to the charge transfer and strong polarization caused by the FCP-like structures.²¹

Oxygen and Hydrogen Evolution Reactions. We then modeled the water splitting reaction using M-PHI as a photocatalyst. Since the VBM of K-PHI lies above the oxidation potential of water, as shown in Figure 3, this material is not suitable for the OER and thus has not been considered for these calculations. The DFT-optimized structures of HO*, O*, and HOO* intermediates on H-PHI, Au-PHI, and Mg-PHI are given in Figure S7 in the SI. The free energy profiles for the OER catalyzed by M-PHI (M = H, Au, and Mg) at 300 K and pH = 0 are given in Figure 5. The curve of the free energy profile should drop lower in each of the steps, from A to D, for the reaction to be thermodynamically favorable. The DFT results suggest that for H-PHI, step A, i.e., formation of HO*, is the rate-limiting step and requires a free energy of 2.40 eV ($U = 0$ V). This is due to the fact that there is no metal atom present to which the water molecule could become adsorbed or activated.⁴⁰ However, interestingly, in Au-PHI and Mg-PHI, the water molecule is adsorbed to the Au and Mg atoms, respectively, as shown in Figure 4. Hence, the free energy of step A decreased to 0.84 and 0.42 eV in Au-PHI and Mg-PHI, respectively. Furthermore, it was found that step C, i.e., formation of HOO*, is the rate-limiting step for Au-PHI and Mg-PHI and requires a free energy of 2.40 and 2.12 eV ($U = 0$ V), respectively. Furthermore, our results suggest that the onset potentials of 2.5, 2.45, and 2.2 V are required for H-PHI, Au-PHI, and Mg-PHI, respectively. The bias (or over-) potentials were then calculated for all three systems and were found to be 1.15, 1.10, and 0.85 V for H-PHI, Au-PHI, and Mg-PHI, respectively. From this, we can now conclude that Mg-PHI would be a better catalyst than H-PHI or Au-PHI. The calculated DFT band gaps of the H-PHI and Mg-PHI, as shown in Table 2, are larger than the onset potentials required to enable decreasing free energy profiles. Thus, excitation of the electrons from the valence band to the conduction band in both H-PHI and Mg-PHI will generate a potential larger than the onset potential, which is sufficient to make all steps, from A to D, thermodynamically feasible. However, in the case of Au-PHI, the onset potential is larger than the computed DFT band gap, which makes this semiconductor as not a suitable photocatalyst for the OER.

The free energy of the HER, which is usually computed as a three-step reaction, using M-PHI as a catalyst was also computed, as shown in Figure 6. The most stable configuration, where one H atom is adsorbed on the M-PHI surface, is given in Figure S8 in the SI. Our DFT results suggest

that the H atom preferentially binds to N atoms of the PHI scaffold in all of the systems studied here. It can be seen from Figure 6 that the free energy of formation of the H* intermediate is positive in all of the cases. The catalyst for which the free energy of formation of the H* intermediate is closer to 0 eV would be more efficient.⁴⁷ It can be concluded from Figure 6 that K-PHI would not be a suitable catalyst for the HER. However, interestingly, our results suggest that both Au-PHI and Mg-PHI would be more efficient HER catalysts than H-PHI.

We also carried out experiments to test the performance of M-PHI as a photocatalyst for the HER, and the results are shown in Figure 7. Our results suggest that except for Ru-PHI, the catalysts are indeed active in HER, which agrees with our theoretical prediction. The narrow band gap of Ru-PHI, as predicted by both DFT and measured by UV–vis spectroscopy, could be the reason why it is not a suitable HER photocatalyst. Figure 7a depicts the rate of H₂ evolution, which is found to be higher when either the white LED or $\lambda = 410$ nm are used rather than $\lambda = 465$ nm in the case of K-PHI, H-PHI, and Mg-PHI photocatalysts. However, in the case of Au-PHI, catalytic performance is only observed with light of $\lambda = 410$ nm. Figure 7b shows the quantum efficiency of the M-PHI photocatalyst in the HER, and it clearly suggests that Mg-PHI is the best-performing HER catalyst, with a quantum efficiency of 7.14%. This agrees with the theoretical prediction of band gap and band edge, the free energy diagram shown in Figure 6, and the spontaneous dissociation of the H₂O molecule upon adsorption.

CONCLUSIONS

By employing DFT calculations and performing laboratory experiments, we have shown here that the 2D CN materials based on ion-exchanged salts of potassium poly(heptazine imide), denoted as M-PHI, are potential photocatalysts for water splitting reactions. The XRD patterns of the M-PHI show that the ions can be exchanged without distorting the crystalline structure. This allows for tuning of the band gaps and band edge potentials to design an effective photocatalyst. Our results suggest that Ru-PHI is not a suitable photocatalyst for water splitting, based on the narrow band gap due to the 4d orbitals of the Ru atom. The OER and HER potentials are straddled between the band edge potentials of H-PHI, Au-PHI, and Mg-PHI. Therefore, these materials are found to be suitable for both the OER and HER. K-PHI, on the other hand, is only active in the HER. We also calculated the free energies of the water splitting reactions with M-PHI applied as catalysts, and they suggest that Mg-PHI would be a better catalyst than the other materials. We also synthesized the M-PHI, and the performance in the HER was verified. Our DFT calculations predict that all of the semiconductors except for Ru-PHI, i.e., (K, H, Au, and Mg)-PHI, are active photocatalysts in the HER. Furthermore, the performance of Mg-PHI in the HER was found to be superior to that of the others, with a rate of 539 $\mu\text{mol}/(\text{h}\cdot\text{g})$ and a quantum efficiency of 7.14% under 410 nm light irradiation. This could be due to activation of the water molecule upon adsorption at Mg-PHI, as predicted by our DFT calculations.

ASSOCIATED CONTENT

Supporting Information

The Supporting Information is available free of charge at <https://pubs.acs.org/doi/10.1021/acs.jpcc.1c03947>.

Figures of computed DFT bulk structures of M-PHI, experimental SEM images and elemental analysis of M-PHI samples, powder X-ray diffraction patterns, UV–vis spectra and ultraviolet photoelectron spectra of M-PHI samples, electronic band structures of M-PHI, effective masses of electrons and holes, and figures of intermediate structures of the OER and HER (PDF)

AUTHOR INFORMATION

Corresponding Author

Thomas D. Kühne – Dynamics of Condensed Matter and Center for Sustainable System Design, Chair of Theoretical Chemistry, University of Paderborn, D-33098 Paderborn, Germany; Paderborn Center for Parallel Computing and Institute for Lightweight Design, University of Paderborn, D-33098 Paderborn, Germany; orcid.org/0000-0001-5471-2407; Email: tdkuehne@mail.uni-paderborn.de

Authors

Sudhir K. Sahoo – Dynamics of Condensed Matter and Center for Sustainable System Design, Chair of Theoretical Chemistry, University of Paderborn, D-33098 Paderborn, Germany; orcid.org/0000-0002-3040-4466

Ivo F. Teixeira – Department of Colloid Chemistry, Max Planck Institute of Colloids and Interfaces, D-14476 Potsdam, Germany; Department of Chemistry, Federal University of São Carlo, 13565-905 São Carlos, SP, Brazil

Aakash Naik – Dynamics of Condensed Matter and Center for Sustainable System Design, Chair of Theoretical Chemistry, University of Paderborn, D-33098 Paderborn, Germany

Julian Heske – Dynamics of Condensed Matter and Center for Sustainable System Design, Chair of Theoretical Chemistry, University of Paderborn, D-33098 Paderborn, Germany; Department of Colloid Chemistry, Max Planck Institute of Colloids and Interfaces, D-14476 Potsdam, Germany

Daniel Cruz – Fritz-Haber-Institut der Max-Planck-Gesellschaft, 14195 Berlin, Germany; Department of Heterogeneous Reactions, Max Planck Institute for Chemical Energy Conversion, 45470 Mülheim an der Ruhr, Germany

Markus Antonietti – Department of Colloid Chemistry, Max Planck Institute of Colloids and Interfaces, D-14476 Potsdam, Germany; orcid.org/0000-0002-8395-7558

Aleksandr Savateev – Department of Colloid Chemistry, Max Planck Institute of Colloids and Interfaces, D-14476 Potsdam, Germany; orcid.org/0000-0002-5760-6033

Complete contact information is available at:

<https://pubs.acs.org/doi/10.1021/acs.jpcc.1c03947>

Notes

The authors declare no competing financial interest.

ACKNOWLEDGMENTS

This project has received funding from the European Research Council (ERC) under the European Union's Horizon 2020 research and innovation programme (Grant Agreement No. 716142). The authors gratefully acknowledge the Gauss Centre for Supercomputing e.V. (www.gausscentre.eu) for funding this project by providing computing time through the John von Neumann Institute for Computing (NIC) on the GCS Supercomputer JUWELS at Jülich Supercomputing Centre (JSC). The generous allocation of computing time by the Paderborn Center for Parallel Computing (PC²) on

OCuLUS and the FPGA-based supercomputer NOCTUA is kindly acknowledged. Dr. I.F.T. thanks CAPES and the Humboldt Foundation for his fellowship.

REFERENCES

- (1) Wang, Q.; Domen, K. Particulate Photocatalysts for Light-Driven Water Splitting: Mechanisms, Challenges, and Design Strategies. *Chem. Rev.* **2020**, *120*, 919–985.
- (2) Maeda, K.; Domen, K. Photocatalytic Water Splitting: Recent Progress and Future Challenges. *J. Phys. Chem. Lett.* **2010**, *1*, 2655–2661.
- (3) Banerjee, T.; Podjaski, F.; Kröger, J.; Biswal, B. P.; Lotsch, B. V. Polymer photocatalysts for solar-to-chemical energy conversion. *Nat. Rev. Mater.* **2021**, *6*, 168–190.
- (4) Takata, T.; Jiang, J.; Sakata, Y.; Nakabayashi, M.; Shibata, N.; Nandal, V.; Seki, K.; Hisatomi, T.; Domen, K. Photocatalytic water splitting with a quantum efficiency of almost unity. *Nature* **2020**, *581*, 411–414.
- (5) Zhang, G.; Lan, Z.-A.; Lin, L.; Lin, S.; Wang, X. Overall water splitting by Pt/g-C₃N₄ photocatalysts without using sacrificial agents. *Chem. Sci.* **2016**, *7*, 3062–3066.
- (6) Berardi, S.; La Ganga, G.; Natali, M.; Bazzan, I.; Puntoriero, F.; Sartorel, A.; Scandola, F.; Campagna, S.; Bonchio, M. Photocatalytic Water Oxidation: Tuning Light-Induced Electron Transfer by Molecular Co₄O₄ Cores. *J. Am. Chem. Soc.* **2012**, *134*, 11104–11107.
- (7) Lin, L.; Lin, Z.; Zhang, J.; Cai, X.; Lin, W.; Yu, Z.; Wang, X. Molecular-level insights on the reactive facet of carbon nitride single crystals photocatalysing overall water splitting. *Nat. Catal.* **2020**, *3*, 649–655.
- (8) Bonchio, M.; Syrgiannis, Z.; Burian, M.; Marino, N.; Pizzolato, E.; Dirian, K.; Rigodanza, F.; Volpato, G. A.; Ganga, G. L.; Demitri, N.; et al. Hierarchical organization of perylene bisimides and polyoxometalates for photo-assisted water oxidation. *Nat. Chem.* **2019**, *11*, 146–153.
- (9) Maeda, K.; Domen, K. New Non-Oxide Photocatalysts Designed for Overall Water Splitting under Visible Light. *J. Phys. Chem. C* **2007**, *111*, 7851–7861.
- (10) Liu, Z.; Hou, W.; Pavaskar, P.; Aykol, M.; Cronin, S. B. Plasmon Resonant Enhancement of Photocatalytic Water Splitting Under Visible Illumination. *Nano Lett.* **2011**, *11*, 1111–1116.
- (11) Chen, S.; Huang, D.; Xu, P.; Xue, W.; Lei, L.; Cheng, M.; Wang, R.; Liu, X.; Deng, R. Semiconductor-based photocatalysts for photocatalytic and photoelectrochemical water splitting: will we stop with photocorrosion? *J. Mater. Chem. A* **2020**, *8*, 2286–2322.
- (12) Iwashina, K.; Iwase, A.; Ng, Y. H.; Amal, R.; Kudo, A. Z-Schematic Water Splitting into H₂ and O₂ Using Metal Sulfide as a Hydrogen-Evolving Photocatalyst and Reduced Graphene Oxide as a Solid-State Electron Mediator. *J. Am. Chem. Soc.* **2015**, *137*, 604–607.
- (13) Lee, S. L.; Chang, C.-J. Recent Progress on Metal Sulfide Composite Nanomaterials for Photocatalytic Hydrogen Production. *Catalysts* **2019**, *9*, No. 457.
- (14) Ray, A.; Sultana, S.; Paramanik, L.; Parida, K. M. Recent advances in phase, size, and morphology-oriented nanostructured nickel phosphide for overall water splitting. *J. Mater. Chem. A* **2020**, *8*, 19196–19245.
- (15) Ong, W.-J.; Tan, L.-L.; Ng, Y. H.; Yong, S.-T.; Chai, S.-P. Graphitic Carbon Nitride (g-C₃N₄)-Based Photocatalysts for Artificial Photosynthesis and Environmental Remediation: Are We a Step Closer To Achieving Sustainability? *Chem. Rev.* **2016**, *116*, 7159–7329.
- (16) Zheng, Y.; Lin, L.; Wang, B.; Wang, X. Graphitic Carbon Nitride Polymers toward Sustainable Photoredox Catalysis. *Angew. Chem., Int. Ed.* **2015**, *54*, 12868–12884.
- (17) Lin, L.; Yu, Z.; Wang, X. Crystalline Carbon Nitride Semiconductors for Photocatalytic Water Splitting. *Angew. Chem., Int. Ed.* **2019**, *58*, 6164–6175.
- (18) Li, T.; Hu, T.; Dai, L.; Li, C. M. Metal-free photo- and electro-catalysts for hydrogen evolution reaction. *J. Mater. Chem. A* **2020**, *8*, 23674–23698.
- (19) Savateev, A.; Pronkin, S.; Epping, J. D.; Willinger, M. G.; Wolff, C.; Neher, D.; Antonietti, M.; Dontsova, D. Potassium Poly(heptazine imides) from Aminotetrazoles: Shifting Band Gaps of Carbon Nitride-like Materials for More Efficient Solar Hydrogen and Oxygen Evolution. *ChemCatChem* **2017**, *9*, 167–174.
- (20) Savateev, A.; Antonietti, M. Ionic Carbon Nitrides in Solar Hydrogen Production and Organic Synthesis: Exciting Chemistry and Economic Advantages. *ChemCatChem* **2019**, *11*, 6166–6176.
- (21) Sahoo, S. K.; Heske, J.; Azadi, S.; Zhang, Z.; Tarakina, N. V.; Oschatz, M.; Khaliullin, R. Z.; Antonietti, M.; Kuehne, T. D. On the Possibility of Helium Adsorption in Nitrogen Doped Graphitic Materials. *Sci. Rep.* **2020**, *10*, No. 5832.
- (22) Chen, Z.; Savateev, A.; Pronkin, S.; Papaefthimiou, V.; Wolff, C.; Willinger, M. G.; Willinger, E.; Neher, D.; Antonietti, M.; Dontsova, D. “The Easier the Better” Preparation of Efficient Photocatalysts-Metastable Poly(heptazine imide) Salts. *Adv. Mater.* **2017**, *29*, No. 1700555.
- (23) Savateev, A.; Pronkin, S.; Willinger, M. G.; Antonietti, M.; Dontsova, D. Towards Organic Zeolites and Inclusion Catalysts: Heptazine Imide Salts Can Exchange Metal Cations in the Solid State. *Chem. - Asian J.* **2017**, *12*, 1517–1522.
- (24) Wang, B. C.; Nisar, J.; Pathak, B.; Kang, T. W.; Ahuja, R. Band gap engineering in BiNbO₄ for visible-light photocatalysis. *Appl. Phys. Lett.* **2012**, *100*, No. 182102.
- (25) Xie, W.; Li, R.; Xu, Q. Enhanced photocatalytic activity of Se-doped TiO₂ under visible light irradiation. *Sci. Rep.* **2018**, *8*, No. 8752.
- (26) Pan, C.; Takata, T.; Kumamoto, K.; Khine Ma, S. S.; Ueda, K.; Minegishi, T.; Nakabayashi, M.; Matsumoto, T.; Shibata, N.; Ikuhara, Y.; et al. Band engineering of perovskite-type transition metal oxynitrides for photocatalytic overall water splitting. *J. Mater. Chem. A* **2016**, *4*, 4544–4552.
- (27) Wang, Y.; Silveri, F.; Bayazit, M. K.; Ruan, Q.; Li, Y.; Xie, J.; Catlow, C. R. A.; Tang, J. Bandgap Engineering of Organic Semiconductors for Highly Efficient Photocatalytic Water Splitting. *Adv. Energy Mater.* **2018**, *8*, No. 1801084.
- (28) Singh, N.; Yadav, D.; Mulay, S. V.; Kim, J. Y.; Park, N.-J.; Baeg, J.-O. Band Gap Engineering in Solvochromic 2D Covalent Organic Framework Photocatalysts for Visible Light-Driven Enhanced Solar Fuel Production from Carbon Dioxide. *ACS Appl. Mater. Interfaces* **2021**, *13*, 14122–14131.
- (29) Hartley, G. O.; Martsinovich, N. Computational design of graphitic carbon nitride photocatalysts for water splitting. *Faraday Discuss.* **2021**, *227*, 341–358.
- (30) Mishra, A.; Mehta, A.; Basu, S.; Shetti, N. P.; Reddy, K. R.; Aminabhavi, T. M. Graphitic carbon nitride (g-C₃N₄)-based metal-free photocatalysts for water splitting: A review. *Carbon* **2019**, *149*, 693–721.
- (31) Blöchl, P. E. Projector augmented-wave method. *Phys. Rev. B* **1994**, *50*, 17953–17979.
- (32) Kresse, G.; Furthmüller, J. Efficiency of ab-initio total energy calculations for metals and semiconductors using a plane-wave basis set. *Comput. Mater. Sci.* **1996**, *6*, 15–50.
- (33) Kresse, G.; Furthmüller, J. Efficient iterative schemes for ab initio total-energy calculations using a plane-wave basis set. *Phys. Rev. B* **1996**, *54*, 11169–11186.
- (34) Kresse, G.; Joubert, D. From ultrasoft pseudopotentials to the projector augmented-wave method. *Phys. Rev. B* **1999**, *59*, 1758–1775.
- (35) Perdew, J. P.; Burke, K.; Ernzerhof, M. Generalized Gradient Approximation Made Simple. *Phys. Rev. Lett.* **1996**, *77*, 3865–3868.
- (36) Grimme, S.; Antony, J.; Ehrlich, S.; Krieg, H. A consistent and accurate ab initio parametrization of density functional dispersion correction (DFT-D) for the 94 elements H-Pu. *J. Chem. Phys.* **2010**, *132*, No. 154104.
- (37) Monkhorst, H. J.; Pack, J. D. Special points for Brillouin-zone integrations. *Phys. Rev. B* **1976**, *13*, 5188–5192.

(38) Heyd, J.; Scuseria, G. E.; Ernzerhof, M. Hybrid functionals based on a screened Coulomb potential. *J. Chem. Phys.* **2003**, *118*, 8207–8215.

(39) Toroker, M. C.; Kanan, D. K.; Alidoust, N.; Isseroff, L. Y.; Liao, P.; Carter, E. A. First principles scheme to evaluate band edge positions in potential transition metal oxide photocatalysts and photoelectrodes. *Phys. Chem. Chem. Phys.* **2011**, *13*, 16644–16654.

(40) Wirth, J.; Neumann, R.; Antonietti, M.; Saalfrank, P. Adsorption and photocatalytic splitting of water on graphitic carbon nitride: a combined first principles and semiempirical study. *Phys. Chem. Chem. Phys.* **2014**, *16*, 15917–15926.

(41) Valdés, Á.; Qu, Z.-W.; Kroes, G.-J.; Rossmeisl, J.; Nørskov, J. K. Oxidation and Photo-Oxidation of Water on TiO₂ Surface. *J. Phys. Chem. C* **2008**, *112*, 9872–9879.

(42) Nørskov, J. K.; Rossmeisl, J.; Logadottir, A.; Lindqvist, L.; Kitchin, J. R.; Bligaard, T.; Jónsson, H. Origin of the Overpotential for Oxygen Reduction at a Fuel-Cell Cathode. *J. Phys. Chem. B* **2004**, *108*, 17886–17892.

(43) Chase, M. W. NIST-JANAF Thermochemical Tables. In *Journal of Physical and Chemical Reference Data*, 4th ed; American Chemical Society: Washington, D.C., 1998.

(44) Zhang, J.; Zhou, P.; Liu, J.; Yu, J. New understanding of the difference of photocatalytic activity among anatase, rutile and brookite TiO₂. *Phys. Chem. Chem. Phys.* **2014**, *16*, 20382–20386.

(45) Shirodkar, S. N.; Waghmare, U. V.; Fisher, T. S.; Grau-Crespo, R. Engineering the electronic bandgaps and band edge positions in carbon-substituted 2D boron nitride: a first-principles investigation. *Phys. Chem. Chem. Phys.* **2015**, *17*, 13547–13552.

(46) Ganose, A. M.; Jackson, A. J.; Scanlon, D. O. sumo: Command-line tools for plotting and analysis of periodic ab initio calculations. *J. Open Source Software* **2018**, *3*, No. 717.

(47) Owens-Baird, B.; Kolen'ko, Y. V.; Kovnir, K. Structure-Activity Relationships for Pt-Free Metal Phosphide Hydrogen Evolution Electrocatalysts. *Chem. - Eur. J.* **2018**, *24*, 7298–7311.